

Cite as: H. Shen *et al.*, *Science*  
10.1126/science.aau2596 (2018).

# Structural basis for the modulation of voltage-gated sodium channels by animal toxins

Huazong Shen<sup>1,2,3\*</sup>, Zhangqiang Li<sup>1,2,3\*</sup>, Yan Jiang<sup>4\*</sup>, Xiaojing Pan<sup>1,2,3\*</sup>, Jianping Wu<sup>1,2,3†</sup>, Ben Cristofori-Armstrong<sup>4</sup>, Jennifer J. Smith<sup>4</sup>, Yanni K. Y. Chin<sup>4</sup>, Jianlin Lei<sup>5</sup>, Qiang Zhou<sup>1,2,3†</sup>, Glenn F. King<sup>4‡</sup>, Nieng Yan<sup>1,2,3†‡</sup>

<sup>1</sup>State Key Laboratory of Membrane Biology, School of Life Sciences and School of Medicine, Tsinghua University, Beijing 100084, China. <sup>2</sup>Beijing Advanced Innovation Center for Structural Biology, School of Life Sciences and School of Medicine, Tsinghua University, Beijing 100084, China. <sup>3</sup>Tsinghua-Peking Joint Center for Life Sciences, School of Life Sciences and School of Medicine, Tsinghua University, Beijing 100084, China. <sup>4</sup>Institute for Molecular Bioscience, The University of Queensland, St. Lucia, Queensland 4072, Australia. <sup>5</sup>Technology Center for Protein Sciences, Ministry of Education Key Laboratory of Protein Sciences, School of Life Sciences, Tsinghua University, Beijing 100084, China.

\*These authors contributed equally to this work. †Present address: Department of Molecular Biology, Princeton University, Princeton, NJ 08540, USA.

‡Corresponding author. Email: nyan@princeton.edu (N.Y.); glenn.king@imb.uq.edu.au (G.F.K.); zhouq2015@mail.tsinghua.edu.cn (Q.Z.)

Animal toxins that modulate the activity of Na<sub>v</sub> channels are broadly divided into two categories—pore blockers and gating modifiers. The pore blockers tetrodotoxin (TTX) and saxitoxin (STX) are responsible for pufferfish and shellfish poisoning in humans, respectively. Here we present structures of the insect Na<sub>v</sub> channel Na<sub>v</sub>PaS bound to a gating modifier toxin Dc1a at 2.8 Å and in the presence of TTX or STX at 2.6 Å and 3.2 Å resolution, respectively. Dc1a inserts into the cleft between VSD<sub>II</sub> and the pore of Na<sub>v</sub>PaS, making key contacts with both domains. The structures with bound TTX or STX reveal the molecular details for the specific blockade of Na<sup>+</sup> access to the selectivity filter from the extracellular side by these guanidinium toxins. The structures shed light on structure-based development of Na<sub>v</sub> channel drugs.

Voltage-gated sodium (Na<sub>v</sub>) channels play a critical role in generating membrane excitability (1), and are targeted by numerous chemical insecticides and human drugs. Na<sub>v</sub> channels are also the most common target of venom neurotoxins. Na<sub>v</sub> channels comprise one single polypeptide chain that folds to four homologous repeats (repeats I-IV), each containing six transmembrane helices designated S1-S6. The S1-S4 segments in each repeat constitute the voltage-sensing domain (VSD), and the S5, S6, and their intervening segments from the four repeats together enclose the ion-conducting pore domain.

While small-molecule neurotoxins such as tetrodotoxin (TTX) and saxitoxin (STX) function as pore blockers, the vast majority of peptidic Na<sub>v</sub> channel toxins are gating modifiers that trap the channel in a particular stage of the gating cycle through interactions with one or more VSDs (2). In contrast to pore blockers, gating modifier toxins (GMTs) have more complex allosteric effects on Na<sub>v</sub> channel function, and they can inhibit (3) or agonise (4) the channel. GMTs, which in general have greater selectivity than pore blockers, are valuable leads for the development of subtype-selective Na<sub>v</sub> channel drugs (3, 5, 6).

Despite extensive studies of the molecular basis by which GMTs modulate Na<sub>v</sub> channel function, no consensus model has emerged of this interaction. Early studies suggested a dominant role for the extracellular S3-S4 loop in GMT binding (7, 8), but subsequent studies have revealed a key role for

the S1-S2 loop in many GMT interactions (4, 9, 10). More recent studies suggest that GMTs nestle into an extracellular-facing cavity between the S1-S4 helices, enabling them to act as a wedge that impedes voltage sensor movement (5, 11). It has been suggested that large GMTs such as those found in scorpion venom might be able to simultaneously contact the VSD and the extracellular loop connecting the pore helix P2 and the S6 segment in pore domain (12), but no studies to date have predicted a role for any of the pore-domain membrane helices in GMT binding.

Small molecules that occlude the pore of Na<sub>v</sub> channels are rare in animal venoms, but TTX and STX are exceptions. As the name indicates, TTX was originally found in tetrodontoid fish exemplified by the pufferfish (fugu). Pufferfish poisoning, resulting from consumption of TTX-containing fish, was documented thousands of years ago in China, Egypt, and later in Japan and Mexico (13, 14). TTX was subsequently shown to be present in venom of the deadly blue-ringed octopus, the poisonous secretions of frogs and newts, and in predatory moon snails; these animals do not synthesize TTX but rather acquire it from endosymbiotic bacteria (15). It was discovered in the mid-20<sup>th</sup> century that the potent toxicity of TTX is due to suppression of action potential generation through specific inhibition of Na<sup>+</sup> influx (14, 16-18). STX is a related guanidinium neurotoxin, produced by marine dinoflagellates and cyanobacteria, that competes with TTX for

binding to Na<sub>v</sub> channels (15). The term saxitoxin is also used to refer to a class of >50 structurally related toxins that are responsible for paralytic shellfish poisoning (19, 20).

Owing to their stringent specificity for Na<sub>v</sub> channels, TTX and STX are widely used for pharmacological characterization of Na<sub>v</sub> channels (21–24). The nine subtypes of mammalian Na<sub>v</sub> channels are classified as TTX-resistant or TTX-sensitive based on their susceptibility to TTX. The latter are inhibited by nanomolar concentrations of TTX, whereas the TTX-resistant subtypes Na<sub>v</sub>1.5, Na<sub>v</sub>1.8, and Na<sub>v</sub>1.9 only respond to micromolar concentrations of the toxin (24, 25). Despite comprehensive studies over the past six decades (26–29), our molecular understanding of the mechanism of action of these toxins has been impeded by the lack of structural information. Crystal structures of several bacterial Na<sub>v</sub> channels have been elucidated (30–32), but these homotetrameric prokaryotic orthologs are insensitive to TTX/STX because they lack the receptor site found in their single-chain, asymmetric eukaryotic counterparts (33).

We recently elucidated the structure of the eukaryotic Na<sub>v</sub> channel Na<sub>v</sub>PaS from American cockroach *Periplaneta americana* at 3.8 Å resolution (34). Here we present a 2.8 Å resolution cryo-EM structure of this channel in complex with Dc1a, a peptidic GMT from venom of the desert bush spider *Duguetia canities* that promotes channel opening of the Na<sub>v</sub> channel from German cockroach (10). We also report cryo-EM structures of the Na<sub>v</sub>PaS-Dc1a complex in the presence of the pore blockers TTX and STX at 2.6 Å and 3.2 Å, respectively. A Na<sup>+</sup> binding site in the selectivity filter (SF) constituted by three carboxylate groups is observed. The structures elucidate the molecular basis for pore blockade by TTX/STX.

## Results

### **Structural determination of Na<sub>v</sub>PaS in complex with Dc1a, TTX, and STX**

Details of cryo-sample preparation, image acquisition, data processing, model building, and structure refinement can be found in Methods. Briefly, micrographs collected on a Titan Krios electron microscope equipped with Gatan K2 Summit detector, GIF Quantum energy filter, and spherical aberration (Cs) image corrector, were used to reconstruct a 3D EM map for the Na<sub>v</sub>PaS-Dc1a complex purified in the presence of 300 mM NaCl to an overall resolution of 2.8 Å. Following a similar protocol, the structures of Na<sub>v</sub>PaS-Dc1a bound to TTX and STX were obtained at 2.6 Å and 3.2 Å, respectively. The central region of Na<sub>v</sub>PaS exhibits higher resolution in all three structures. Application of a mask for the central region during post-processing further improved the resolution of this region to 2.7 Å for Na<sub>v</sub>PaS-Dc1a, and 3.1 Å for Na<sub>v</sub>PaS-Dc1a-STX, while that for Na<sub>v</sub>PaS-Dc1a-TTX remained at 2.6 Å (Fig. 1, A and B, figs. S1 to S4, and table S1). The excellent quality of the EM maps ensured reliable assignment of the

ligands and surrounding residues. All residues of the selectivity filter (SF), including the invariant residues from the four repeats, Asp/Glu/Lys/Ala (DEKA), and surrounding segments are unambiguously resolved in the high-resolution EM reconstructions (Fig. 1C and fig. S4).

### **VSD<sub>II</sub> and the pore domain together accommodate Dc1a**

The structure of the Dc1a-Na<sub>v</sub>PaS complex (Fig. 2, A to C) confirms that VSD<sub>II</sub> constitutes the primary docking site for Dc1a, as we reported previously (10). Comparison with the ligand-free Na<sub>v</sub>PaS structure (34) reveals minor conformational changes in the channel upon Dc1a binding, mainly affecting VSD<sub>II</sub> (fig. S5). In contrast, the structure of Dc1a undergoes considerable rearrangement (Fig. 2B). The NMR structure of Dc1a alone contains five short β strands that are organized into an N-terminal β-sheet and a C-terminal inhibitor cystine knot (knottin) motif (10). In the complex, however, the two C-terminal β strands extend into the previously unstructured connecting loop region to form an elongated β-hairpin that inserts deeply into the extracellular cavity enclosed by the four segments in VSD<sub>II</sub> and the adjacent pore-forming S5 segment from repeat III (S5<sub>III</sub>) (Fig. 2, A and B).

Dc1a makes extensive polar and hydrophobic interactions with Na<sub>v</sub>PaS that are more complex than predicted by any model of GMT binding, involving interactions with the S1-S2 loop (the loop that connects S1 and S2), the gating charge on S4, the extracellular pore loops, and the S5 pore-domain helix of repeat III. The toxin makes no interactions with the S3-S4 loop. The edge of the β sheet of Dc1a interacts with the short extracellular helix in repeat III above the pore domain (designated Eα<sub>III</sub>) (Fig. 2B); specifically Tyr33 and Asp56 on Dc1a interact with His1032 and Arg1027 on Na<sub>v</sub>PaS, respectively (Fig. 2C, left). On one side of the VSD<sub>II</sub> cavity, the toxin interacts extensively with the S1-S2 loop (designated L1-2<sub>II</sub>); in particular, the guanidinium group of Dc1a-Arg41 interacts with the main chain carbonyl oxygen and the side chain carboxyl group of Asp542 (Fig. 2C, middle).

The β3-β4 hairpin of Dc1a inserts deep into the VSD<sub>II</sub> cavity, with Phe47 and Phe48 at the tip of the hairpin surrounded by hydrophobic residues from S1<sub>II</sub> and the side wall of the pore domain involving S5<sub>III</sub>. Meanwhile, the aromatic ring of Dc1a-Phe48 makes a π-cation interaction with the gating-charge residue Arg613 (R3) (Fig. 2C, right). Gln1002 on S5<sub>III</sub> makes extensive polar interactions with the side chain of Dc1a-Lys44 and the backbone amide of Dc1a-Phe48. These specific interactions with both VSD<sub>II</sub> and the pore domain collectively stabilize VSD<sub>II</sub> in the “up” state, consistent with Dc1a inducing opening of the channel (10).

We investigated the importance of these intermolecular interactions by examining the effect of toxin and channel mutations using the orthologous Na<sub>v</sub>Bg channel from the German cockroach *Blattella germanica* (Fig. 2, D and E). Na<sub>v</sub>Bg

is potently activated by Dc1a but, unlike Na<sub>v</sub>PaS, it is amenable to electrophysiological analysis (10). Modulation of Na<sub>v</sub>Bg activity by Dc1a was almost abolished when residues Asp21, Tyr33, Arg41, Lys44, and Asp56 were mutated to Ala, while Phe47A, Phe48A, and S49A mutations severely diminished but did not completely abrogate Dc1a activity (Fig. 2D and fig. S6). Based on <sup>1</sup>H NMR chemical shifts, none of these mutations perturb the structure of Dc1a (figs. S7 and S8), thus we conclude that they all contribute to Dc1a modulation of insect Na<sub>v</sub> channels.

Mutation of Na<sub>v</sub>Bg residues involved in Dc1a binding caused minor shifts in the conductance-voltage (G-V) relationship for the channel (fig. S9). Thus, for each channel mutant, we quantified the previously noted ability of Dc1a to induce a hyperpolarizing shift ( $\Delta_{G-V}$ ) in the G-V relationship (10), thereby allowing each mutant channel to serve as its own control (Fig. 2E and fig. S9). Both conservative (D→E) and harsher (D→A) mutations of Asp805 and Asp808 in L1-2<sub>II</sub> (corresponding to Asp539 and Asp542 in Na<sub>v</sub>PaS) greatly reduced  $\Delta_{G-V}$ , highlighting the critical importance of these residues to Dc1a binding. Notably, neither residue is conserved in mammalian Na<sub>v</sub> channels (34), providing a molecular rationale for the insect selectivity of Dc1a (10). Mutation of R1447K in E $\alpha$ III (R1027 in Na<sub>v</sub>PaS) reduced Dc1a activity, providing support for this unexpected toxin-channel interaction, whereas mutation of His1452 in E $\alpha$ III (His1032 in Na<sub>v</sub>PaS) had minimal impact. Consistent with the cryo-EM structure (Fig. 2C), mutation of Arg876 (Arg610 in Na<sub>v</sub>PaS), one of the uppermost gating charge residues, had minimal impact on Dc1a activity, indicating that this residue is not crucial for the Dc1a-Na<sub>v</sub>PaS interaction. Finally, a conservative mutation of Gln1422 (Q1002 in Na<sub>v</sub>PaS) on S5<sub>III</sub> to Asn greatly reduced toxin activity (Fig. 2E), consistent with the interactions observed between this pore-helix residue and residues Lys44 and Phe48 in Dc1a (Fig. 2C). Notably, the corresponding residue is Asn in human Na<sub>v</sub>1.1-1.8 and Tyr in Na<sub>v</sub>1.9; again consistent with the insect selectivity of Dc1a (10).

In summary, the mutagenesis data provide strong support for the physiological relevance of the complex network of intermolecular interactions observed in the Dc1a-Na<sub>v</sub>PaS structure.

### Recognition of TTX

TTX and STX, both of which have the molecular weight ~300 Da, are clearly resolved in the cryo-EM reconstructions (Figs. 3 and 4 and fig. S4). TTX contains one guanidinium, two ether bonds, one oxygen anion, and multiple hydroxyl groups (Fig. 3A and fig. S4A). At lower pH, the oxygen anion is protonated. The map also reveals a density that likely belongs to a coordinated Na<sup>+</sup> (fig. S4C), which we discuss further below.

TTX blocks the entrance to the selectivity filter (SF) vestibule through an extensive network of electrostatic interactions. The invariant acidic residues on the corresponding locus of the P2 segment in repeats I, II, and IV each form multiple hydrogen bonds or salt bridges with the polar groups of TTX (Fig. 3, B to D). Asp375 and Glu701 in the DEKA motif also directly contribute to TTX binding (Fig. 3C). Three consecutive backbone amides of the residues that demarcate the P2 helix from the preceding SF loop in repeat III simultaneously bind to C10-OH and the oxygen atom of the ether bond between C7 and C10, while Trp1063 and the carbonyl oxygen of Phe1060 coordinate C9-OH (Fig. 3, B and C).

All of the aforementioned residues are invariant in human Na<sub>v</sub> channels (Fig. 3D). Tyr376 on repeat I is positioned adjacent to the guanidinium group in TTX, enabling it to make  $\pi$ -cation interactions with the toxin (Fig. 3, B and C). The corresponding locus is occupied by either Phe or Tyr in TTX-sensitive Na<sub>v</sub> channel subtypes, but replaced by Cys or Ser in the TTX-resistant subtypes Na<sub>v</sub>1.5, Na<sub>v</sub>1.8, and Na<sub>v</sub>1.9 (Fig. 3D). The structure therefore explains why substitution of Cys with Tyr at this position in Na<sub>v</sub>1.5 confers TTX sensitivity (24, 35-37). The position after the invariant Glu on the first helical turn of P2<sub>I</sub> is occupied by Arg or Lys in TTX-resistant subtypes, whereas an Asn residue occupies this locus in TTX-sensitive channels (Fig. 3D). Although this residue is too far away to directly participate in TTX coordination, a basic residue at this site may reduce the local electronegativity and further lower channel affinity for TTX.

### Recognition of STX

The functional groups of STX include the 1,2,3- and 7,8,9- guanidinium groups, the C12 hydroxyls (C12-OHs), and the 13-carbamoyl group. The distinctive shape of this small molecule allows reliable structural assignment (Fig. 4A and fig. S4, B and D). Polar and charged residues from all four repeats that are positioned at the outer entrance to the SF form extensive interactions with the functional groups of STX (Fig. 4, A and B).

The acidic residues on the first helical turn of the P2 helix in each repeat, which together constitute the outer electro-negative ring, provide the primary docking site for STX. The 7,8,9- and 1,2,3-guanidinium groups are respectively bound to the invariant Glu residues on the P2 helix in repeats I and II, while the carbamoyl and the C12-OH are coordinated by polar groups in repeat III and the invariant Asp in repeat IV, respectively. Tyr376 in repeat I contributes to coordination of the toxin through  $\pi$ -cation interaction with the 1,2,3-guanidinium group of STX (Fig. 4B). The carbonyl oxygen in the carbamoyl group and one adjacent C12-OH are hydrogen-bonded to the backbone amide of the invariant Gly (Gly1062 in Na<sub>v</sub>PaS) in repeat III. The DEKA-motif residue Glu701 in repeat II forms a hydrogen bond with N7 of STX (Fig. 4B, right).

All of the STX-coordinating residues in Na<sub>v</sub>PaS, except for Tyr376 and Gln1065, are conserved in mammalian Na<sub>v</sub> channels (Fig. 4C). The corresponding residue for Na<sub>v</sub>PaS-Gln1065 is Asp in all human Na<sub>v</sub> subtypes except Na<sub>v</sub>1.7, where this position is occupied by Ile. The Na<sub>v</sub>PaS-STX structure provides a molecular basis for the lower affinity of STX for Na<sub>v</sub>1.7 than for Na<sub>v</sub>1.4 (38) as replacement of Gln with a hydrophobic Ile at this locus would lead to a loss of electrostatic interactions with the carbamoyl amine of STX (Fig. 4, B and C).

### **Molecular mechanism for pore blockade by TTX/STX**

The cryo-EM structures of Na<sub>v</sub>PaS in complex with TTX or STX reveal the details of their interaction with the channel. However, elucidation of their mechanism of action also requires a molecular understanding of Na<sup>+</sup> permeation through the SF. Our recent molecular dynamics (MD) simulation of the pore domain of Na<sub>v</sub>PaS suggests a preferred path involving the acidic residues from repeats I & II (39) (fig. S10). Examination of the EM map for the Na<sub>v</sub>PaS-Dc1a complex, which was purified in the presence of 300 mM NaCl, identified a strong density encaged by three acidic residues, Asp375 and Glu701 from the DEKA motif and Glu704 on P2<sub>II</sub>, which is positioned above Glu701 (Fig. 5A). Coordination of this density is nearly identical to that observed in the 2.6 Å reconstruction of the Na<sub>v</sub>PaS-Dc1a-TTX complex purified in 150 mM NaCl (fig. S4C). The stable conformation of the three carboxylate side chains suggests that they may be stabilized by a cation. The density therefore likely belongs to a Na<sup>+</sup> ion rather than a water molecule. In addition, this site coincides with the energetic minimum observed in the MD simulation of Na<sup>+</sup> penetration through the SF of Na<sub>v</sub>PaS. We therefore assigned a Na<sup>+</sup> ion to this density and refer to this Na<sup>+</sup> binding site as the “DEE site” (Fig. 5A).

The preference of Na<sup>+</sup> for the DEE site can be explained by the distinct chemical compositions of the four repeats (Fig. 5B, left). The invariant Arg on P2<sub>II</sub> (Arg696 in Na<sub>v</sub>PaS), the Lys in the DEKA motif on repeat III, and a hydrophobic residue on P2<sub>III</sub> (Leu1064 in Na<sub>v</sub>PaS and Met in human Na<sub>v</sub> channels) may together repel cations to the DEE site (Fig. 5B and fig. S10). Placement of TTX or STX at the entrance to the SF vestibule preserves the configuration of the DEE site, but completely blocks access of Na<sup>+</sup> to this site from the extracellular milieu (Fig. 5B).

### **Summary**

In this study, we report the structures of a eukaryotic Na<sub>v</sub> channel, Na<sub>v</sub>PaS, in complex with three natural toxins. The structures of Na<sub>v</sub>PaS in complex with the well-characterized neurotoxins TTX and STX provide a molecular explanation for a wealth of functional studies (39–48). It is noteworthy that the molecular weights of TTX and STX are both around 300 Da. The clear resolution of these small molecules bound

to a Na<sub>v</sub> channel with datasets collected in just a few days showcases the power of cryo-EM, which is likely to play an increasingly important role in structure-aided drug discovery.

The structure of the Na<sub>v</sub>PaS-Dc1a complex confirmed the important role of VSD<sub>II</sub> in binding this GMT. However, it also revealed that the network of intermolecular interactions is much more complex than previously anticipated, with key interactions between the toxin and both the S5<sub>III</sub> pore-domain helix and the extracellular dome above the pore. Thus, one has to apply caution when using isolated Na<sub>v</sub> channel VSDs for drug discovery or for understanding the molecular basis of GMT action. Finally, the recently determined structure of the EeNa<sub>v</sub>1.4-β1 complex revealed that the extracellular dome provides a docking site for β subunits (49), which together with the current structure might explain why the sensitivity of Na<sub>v</sub> channels to some GMTs is modulated by the presence of an accessory β subunit (50).

### **Materials and methods**

#### **Purification of Na<sub>v</sub>PaS in complex with toxins**

Recombinant Na<sub>v</sub>PaS and Dc1a proteins were expressed and purified as reported (10, 34). To assemble the complex, Dc1a (40 μM) was added to the concentrated Na<sub>v</sub>PaS solution and incubated at 4°C for 0.5 hours before size exclusion chromatography (SEC, Superose® 6 10/300 GL GE Healthcare). For Na<sub>v</sub>PaS-Dc1a complexes bound to TTX or STX, TTX (50 μM) or STX (4 μM) were respectively added to the concentrated Na<sub>v</sub>PaS solution 15 min before adding Dc1a. The peak fractions of size exclusion chromatography were pooled and concentrated to approximately 2 mg/ml. For the sample without TTX or STX, 300 mM NaCl was used during purification while for the sample with TTX or STX, 150 mM NaCl was used.

#### **Production of Dc1a analogs**

Plasmids encoding Dc1a mutants were generated via PCR-based mutagenesis using a plasmid encoding wild-type Dc1a [pLIC-NSB3; (10)] as template. The DNA sequence of all mutants was confirmed by Sanger sequencing. Peptide concentrations were determined by calculating the area under the RP-HPLC peak (at 214 nm) of all analogs, then comparing these to the peak area obtained from a Dc1a standard whose concentration had been determined by amino acid analysis.

#### **Cryo-EM data acquisition**

Cryo-EM samples were prepared as described (34). In brief, aliquots (3.5 μl) of freshly purified Na<sub>v</sub>PaS complex were placed on glow-discharged holey carbon grids (Quantifoil Cu R1.2/1.3), which were blotted for 3.5 s and flash-frozen in liquid ethane cooled by liquid nitrogen with a Vitrobot Mark IV (Thermo Fisher Scientific Inc.). The grids were subsequently

transferred to a Titan Krios (Thermo Fisher Scientific Inc.) electron microscopy operating at 300 kV equipped with Cs-corrector (Thermo Fisher Scientific Inc.), Gatan K2 Summit detector and GIF Quantum energy filter. A total of 2,764, 3,050 or 4,539 movie stacks, for Na<sub>v</sub>PaS-Dc1a complex, TTX or STX-supplemented samples respectively, were automatically collected using AutoEMation (51) with a slit width of 20 eV on the energy filter and a preset defocus range from -1.8 μm to -1.5 μm in super-resolution mode at a nominal magnification of 105,000 X. Each stack was exposed for 5.6 s with an exposing time of 0.175 s per frame, resulting in a total of 32 frames per stack. The total dose rate was about 48 e/Å<sup>2</sup> for each stack. The stacks were motion corrected with MotionCor2 (52) and binned 2-fold, resulting in a pixel size of 1.091 Å/pixel. Meanwhile, dose weighting was performed (53). The defocus values were estimated with Gctf (54).

### Image processing

The procedure for data processing is summarized in fig. S2. A total of 895,227, 1,506,774, or 1,211,302 particles, for Na<sub>v</sub>PaS-Dc1a complex, TTX or STX-supplemented samples respectively, were automatically picked using RELION (55–58) and Gautomatch (K. Zhang, [www.mrc-lmb.cam.ac.uk/kzhang/](http://www.mrc-lmb.cam.ac.uk/kzhang/)). After 2D classification, a total of 838,471, 1,042,430 or 447,993 particles were selected for the Na<sub>v</sub>PaS-Dc1a complex, TTX or STX-supplemented samples and subjected to global angular searching 3D classification with only one class. For each of the last several iterations of the global angular searching 3D classification, a local angular searching 3D classification was performed, during which the particles were classified into 4 classes. A total of non-duplicated 595,020, 742,093 or 378,538 particles were selected from the local angular searching 3D classification for Na<sub>v</sub>PaS-Dc1a complex, TTX or STX-supplemented samples, respectively. For Na<sub>v</sub>PaS-Dc1a complex and STX-supplemented samples, the particles were subjected to multi-reference classification to remove bad particles. Then the good particles were subjected to 3D auto-refinement with 255,265, 742,093, or 166,805 particles for Na<sub>v</sub>PaS-Dc1a complex, TTX or STX-supplemented samples, respectively. The 3D auto-refinements were further optimized with a larger box size of 320 pixels and local defocus values determined with Gctf. Finally, a local mask was applied during postprocessing to improve the local resolution of pore domain. 2D classification, 3D classification and auto-refinement were performed with RELION 2.1. The resolution was estimated with the gold-standard Fourier shell correlation 0.143 criterion (59) with high resolution noise substitution (60).

### Model building and structure refinement

Model building was first carried out based on the 2.9 Å re-

construction map of the Na<sub>v</sub>PaS-Dc1a complex. The structures of Na<sub>v</sub>PaS and Dc1a (PDB accession codes: 5X0M and 2MI5, respectively) were fitted into the EM map by CHIMERA (61). Afterwards, the fitted models were manually adjusted in COOT (62).

In total, 1,380 residues were built with 1,272 side chains assigned for the structure. In addition, 7 sugar and 2 lipid moieties were assigned. The intracellular I-II linker, II-III linker, the N-terminal sequence preceding the NTD, and the C-terminal segment following the CTD were not modeled due to the lack of corresponding densities.

The model of Na<sub>v</sub>PaS-Dc1a-STX complex was generated using the structure of the Na<sub>v</sub>PaS-Dc1a complex as the starting model, which was fitted into the 3.2 Å 3D reconstruction map. 3D conformer of STX (PubChem CID: 37165) was processed with phenix.elbow application in PHENIX (63) and the resulted structure can be fitted into the map unambiguously in COOT. The docked models and residues were manually adjusted in COOT.

The model of Na<sub>v</sub>PaS-Dc1a-TTX complex was generated using the structure of the Na<sub>v</sub>PaS-Dc1a-STX complex as a starting model, which was fitted into the 2.6 Å 3D reconstruction map. The 3D structure of TTX (PubChem CID: 11174599) was used to replace STX. Every residue was manually checked in COOT.

Structure refinement was performed using phenix.real\_space\_refine application in PHENIX in real space with secondary structure and geometry restraints to prevent structure over-fitting. Over-fitting of the overall model was monitored by refining the model in one of the two independent maps from the gold-standard refinement approach and testing the refined model against the other map (64) (fig. S1D). Statistics of the map reconstruction and model refinement can be found in table S1.

### Electrophysiology

Channel mutants were generated using PCR-based mutagenesis with Na<sub>v</sub>Bg (65) as template, then confirmed by DNA sequencing. Fragments from these mutant clones were excised and cloned back into the original Na<sub>v</sub>Bg containing plasmid to produce final mutant constructs. The DNA sequence of all constructs was confirmed by Sanger sequencing and cRNA synthesized using T7 polymerase (mMessage mMachin kit, Life Technologies, USA) after linearizing the DNA with *NotI* restriction enzyme. *Xenopus laevis* oocytes were injected with cRNA (0.5–4 ng depending on the channel) encoding wild-type or mutant Na<sub>v</sub>Bg together with the TipE subunit (66) (1:5 molar ratio), then they were incubated at 17°C in ND96 solution (in mM: 96 NaCl, 2 KCl, 1.8 CaCl<sub>2</sub>, 2 MgCl<sub>2</sub> and 5 HEPES; pH 7.6) supplemented with 5 mM pyruvic acid, 50 μg/mL gentamicin sulfate, and 2.5% horse serum. Currents

were recorded 1–3 days after injections using the two-electrode voltage-clamp technique (Axoclamp 900A, Molecular Devices, USA) with a 30  $\mu\text{l}$  recording chamber. Microelectrodes were filled with 3 M KCl and resistances were 0.5–1 M $\Omega$ . All experiments were performed at room temperature ( $\sim 21^\circ\text{C}$ ) in ND96 solution containing 0.1% fatty-acid free bovine serum albumin to prevent adsorption of peptides to plastic. After addition of peptides to the recording chamber, equilibration between peptide and channel was monitored using weak depolarizations elicited at 5 s intervals. For all recordings, voltage-activation relationships were recorded in the absence and presence of peptide. To determine conductance-voltage relationships, oocytes were held at  $-90$  mV and depolarized in 5-mV steps from  $-90$  mV to  $+30$  mV for 50 ms. Data were digitized at 20 kHz; leak and background conductance were identified by blocking channels with TTX and subtracting background currents. Data analyses were performed using Clampfit 10.5 (Molecular Devices, USA) and Prism 7 (GraphPad Software, USA).

## REFERENCES AND NOTES

- B. Hille, *Ion Channels of Excitable Membranes* (Sinauer Associates, ed. 3, 2001), vol. 1, pp. 814.
- J. Kalia, M. Milescu, J. Salvatierra, J. Wagner, J. K. Klint, G. F. King, B. M. Olivera, F. Bosmans, From foe to friend: Using animal toxins to investigate ion channel function. *J. Mol. Biol.* **427**, 158–175 (2015). [doi:10.1016/j.jmb.2014.07.027](https://doi.org/10.1016/j.jmb.2014.07.027) [Medline](#)
- J. R. Deuis, Z. Dekan, J. S. Wingerd, J. J. Smith, N. R. Munasinghe, R. F. Bhola, W. L. Imlach, V. Herzig, D. A. Armstrong, K. J. Rosengren, F. Bosmans, S. G. Waxman, S. D. Dib-Hajj, P. Escoubas, M. S. Minett, M. J. Christie, G. F. King, P. F. Alewood, R. J. Lewis, J. N. Wood, I. Vetter, Pharmacological characterisation of the highly  $\text{Na}_v1.7$  selective spider venom peptide Pn3a. *Sci. Rep.* **7**, 40883 (2017). [doi:10.1038/srep40883](https://doi.org/10.1038/srep40883) [Medline](#)
- J. D. Osteen, V. Herzig, J. Gilchrist, J. J. Emrick, C. Zhang, X. Wang, J. Castro, S. Garcia-Caraballo, L. Grundy, G. Y. Rychkov, A. D. Weyer, Z. Dekan, E. A. B. Undheim, P. Alewood, C. L. Stucky, S. M. Brierley, A. I. Basbaum, F. Bosmans, G. F. King, D. Julius, Selective spider toxins reveal a role for the  $\text{Na}_v1.1$  channel in mechanical pain. *Nature* **534**, 494–499 (2016). [doi:10.1038/nature17976](https://doi.org/10.1038/nature17976) [Medline](#)
- N. A. Minassian, A. Gibbs, A. Y. Shih, Y. Liu, R. A. Neff, S. W. Sutton, T. Mirzadegan, J. Connor, R. Fellows, M. Husovsky, S. Nelson, M. J. Hunter, M. Flinspach, A. D. Wickenden, Analysis of the structural and molecular basis of voltage-sensitive sodium channel inhibition by the spider toxin huwentoxin-IV ( $\mu\text{-TRTX-Hh2a}$ ). *J. Biol. Chem.* **288**, 22707–22720 (2013). [doi:10.1074/jbc.M113.461392](https://doi.org/10.1074/jbc.M113.461392) [Medline](#)
- J. K. Murray, J. Ligutti, D. Liu, A. Zou, L. Poppe, H. Li, K. L. Andrews, B. D. Moyer, S. I. McDonough, P. Favreau, R. Stöcklin, L. P. Miranda, Engineering potent and selective analogues of GpTx-1, a tarantula venom peptide antagonist of the  $\text{Na}_v1.7$  sodium channel. *J. Med. Chem.* **58**, 2299–2314 (2015). [doi:10.1021/jm501765v](https://doi.org/10.1021/jm501765v) [Medline](#)
- S. Cestèle, Y. Qu, J. C. Rogers, H. Rochat, T. Scheuer, W. A. Catterall, Voltage sensor-trapping: Enhanced activation of sodium channels by  $\beta$ -scorpion toxin bound to the S3-S4 loop in domain II. *Neuron* **21**, 919–931 (1998). [Medline](#)
- F. Bosmans, M. F. Martin-Eauclaire, K. J. Swartz, Deconstructing voltage sensor function and pharmacology in sodium channels. *Nature* **456**, 202–208 (2008). [doi:10.1038/nature07473](https://doi.org/10.1038/nature07473) [Medline](#)
- J. Wang, V. Yarov-Yarovoy, R. Kahn, D. Gordon, M. Gurevitz, T. Scheuer, W. A. Catterall, Mapping the receptor site for  $\alpha$ -scorpion toxins on a  $\text{Na}^+$  channel voltage sensor. *Proc. Natl. Acad. Sci. U.S.A.* **108**, 15426–15431 (2011). [doi:10.1073/pnas.1112320108](https://doi.org/10.1073/pnas.1112320108) [Medline](#)
- N. S. Bende, S. Dziemborowicz, M. Mobli, V. Herzig, J. Gilchrist, J. Wagner, G. M. Nicholson, G. F. King, F. Bosmans, A distinct sodium channel voltage-sensor locus determines insect selectivity of the spider toxin Dcla. *Nat. Commun.* **5**, 4350 (2014). [doi:10.1038/ncomms5350](https://doi.org/10.1038/ncomms5350) [Medline](#)
- C. H. Lau, G. F. King, M. Mobli, Molecular basis of the interaction between gating modifier spider toxins and the voltage sensor of voltage-gated ion channels. *Sci. Rep.* **6**, 34333 (2016). [doi:10.1038/srep34333](https://doi.org/10.1038/srep34333) [Medline](#)
- J. Z. Zhang, V. Yarov-Yarovoy, T. Scheuer, I. Karbat, L. Cohen, D. Gordon, M. Gurevitz, W. A. Catterall, Mapping the interaction site for a  $\beta$ -scorpion toxin in the pore module of domain III of voltage-gated  $\text{Na}^+$  channels. *J. Biol. Chem.* **287**, 30719–30728 (2012). [doi:10.1074/jbc.M112.370742](https://doi.org/10.1074/jbc.M112.370742) [Medline](#)
- H. S. Mosher, F. A. Fuhrman, H. D. Buchwald, H. G. Fischer, Tarichatoxin-tetrodotoxin: A potent neurotoxin. *Science* **144**, 1100–1110 (1964). [doi:10.1126/science.144.3622.1100](https://doi.org/10.1126/science.144.3622.1100) [Medline](#)
- C. Y. Kao, Tetrodotoxin, saxitoxin and their significance in the study of excitation phenomena. *Pharmacol. Rev.* **18**, 997–1049 (1966). [Medline](#)
- L. M. Durán-Riveroll, A. D. Cembella, Guanidinium toxins and their interactions with voltage-gated sodium ion channels. *Mar. Drugs* **15**, 303 (2017). [doi:10.3390/md15100303](https://doi.org/10.3390/md15100303) [Medline](#)
- J. H. Fleisher, P. J. Killos, C. S. Harrison, Effects of puffer poison on neuromuscular transmission. *J. Pharmacol. Exp. Ther.* **133**, 98–105 (1961). [Medline](#)
- T. Narahashi, J. W. Moore, W. R. Scott, Tetrodotoxin blockage of sodium conductance increase in lobster giant axons. *J. Gen. Physiol.* **47**, 965–974 (1964). [doi:10.1085/jgp.47.5.965](https://doi.org/10.1085/jgp.47.5.965) [Medline](#)
- W. S. Agnew, S. R. Levinson, J. S. Brabson, M. A. Raftery, Purification of the tetrodotoxin-binding component associated with the voltage-sensitive sodium channel from *Electrophorus electricus* electroplax membranes. *Proc. Natl. Acad. Sci. U.S.A.* **75**, 2606–2610 (1978). [doi:10.1073/pnas.75.6.2606](https://doi.org/10.1073/pnas.75.6.2606) [Medline](#)
- H. Sommer, K. F. Meyer, Mussel poisoning. *Cal. West. Med.* **42**, 423–426 (1935). [Medline](#)
- J. F. Lawrence, B. Niedzwiedek, C. Menard, Quantitative determination of paralytic shellfish poisoning toxins in shellfish using prechromatographic oxidation and liquid chromatography with fluorescence detection: Collaborative study. *J. AOAC Int.* **88**, 1714–1732 (2005). [Medline](#)
- S. Hagiwara, S. Nakajima, Differences in Na and Ca spikes as examined by application of tetrodotoxin, procaine, and manganese ions. *J. Gen. Physiol.* **49**, 793–806 (1966). [doi:10.1085/jgp.49.4.793](https://doi.org/10.1085/jgp.49.4.793) [Medline](#)
- J. K. Reed, M. A. Raftery, Properties of the tetrodotoxin binding component in plasma membranes isolated from *Electrophorus electricus*. *Biochemistry* **15**, 944–953 (1976). [doi:10.1021/bi00650a002](https://doi.org/10.1021/bi00650a002) [Medline](#)
- T. Clairfeuille, H. Xu, C. M. Koth, J. Payandeh, Voltage-gated sodium channels viewed through a structural biology lens. *Curr. Opin. Struct. Biol.* **45**, 74–84 (2017). [doi:10.1016/j.sbi.2016.11.022](https://doi.org/10.1016/j.sbi.2016.11.022) [Medline](#)
- J. Satin, J. W. Kyle, M. Chen, P. Bell, L. L. Cribbs, H. A. Fozzard, R. B. Rogart, A mutant of TTX-resistant cardiac sodium channels with TTX-sensitive properties. *Science* **256**, 1202–1205 (1992). [doi:10.1126/science.256.5060.1202](https://doi.org/10.1126/science.256.5060.1202) [Medline](#)
- N. T. Blair, B. P. Bean, Roles of tetrodotoxin (TTX)-sensitive  $\text{Na}^+$  current, TTX-resistant  $\text{Na}^+$  current, and  $\text{Ca}^{2+}$  current in the action potentials of nociceptive sensory neurons. *J. Neurosci.* **22**, 10277–10290 (2002). [doi:10.1523/JNEUROSCI.22-23.10277.2002](https://doi.org/10.1523/JNEUROSCI.22-23.10277.2002) [Medline](#)
- S. Cestèle, W. A. Catterall, Molecular mechanisms of neurotoxin action on voltage-gated sodium channels. *Biochimie* **82**, 883–892 (2000). [doi:10.1016/S0300-9084\(00\)01174-3](https://doi.org/10.1016/S0300-9084(00)01174-3) [Medline](#)
- G. M. Lipkind, H. A. Fozzard, A structural model of the tetrodotoxin and saxitoxin binding site of the  $\text{Na}^+$  channel. *Biophys. J.* **66**, 1–13 (1994). [doi:10.1016/S0006-3495\(94\)80746-5](https://doi.org/10.1016/S0006-3495(94)80746-5) [Medline](#)
- B. Hille, The receptor for tetrodotoxin and saxitoxin. A structural hypothesis. *Biophys. J.* **15**, 615–619 (1975). [doi:10.1016/S0006-3495\(75\)85842-5](https://doi.org/10.1016/S0006-3495(75)85842-5) [Medline](#)
- A. P. Thottumkara, W. H. Parsons, J. Du Bois, Saxitoxin. *Angew. Chem. Int. Ed.* **53**, 5760–5784 (2014). [doi:10.1002/anie.201308235](https://doi.org/10.1002/anie.201308235) [Medline](#)
- J. Payandeh, T. Scheuer, N. Zheng, W. A. Catterall, The crystal structure of a voltage-gated sodium channel. *Nature* **475**, 353–358 (2011). [doi:10.1038/nature10238](https://doi.org/10.1038/nature10238) [Medline](#)
- X. Zhang, W. Ren, P. DeCaen, C. Yan, X. Tao, L. Tang, J. Wang, K. Hasegawa, T. Kumasaka, J. He, J. Wang, D. E. Clapham, N. Yan, Crystal structure of an orthologue of the NaChBac voltage-gated sodium channel. *Nature* **486**, 130–134 (2012). [doi:10.1038/nature11054](https://doi.org/10.1038/nature11054) [Medline](#)
- E. C. McCusker, C. Bagnérís, C. E. Naylor, A. R. Cole, N. D'Avanzo, C. G. Nichols, B.

- A. Wallace, Structure of a bacterial voltage-gated sodium channel pore reveals mechanisms of opening and closing. *Nat. Commun.* **3**, 1102 (2012). [doi:10.1038/ncomms2077](https://doi.org/10.1038/ncomms2077) [Medline](#)
33. D. Ren, B. Navarro, H. Xu, L. Yue, Q. Shi, D. E. Clapham, A prokaryotic voltage-gated sodium channel. *Science* **294**, 2372–2375 (2001). [doi:10.1126/science.1065635](https://doi.org/10.1126/science.1065635) [Medline](#)
34. H. Shen, Q. Zhou, X. Pan, Z. Li, J. Wu, N. Yan, Structure of a eukaryotic voltage-gated sodium channel at near-atomic resolution. *Science* **355**, eaal4326 (2017). [doi:10.1126/science.aal4326](https://doi.org/10.1126/science.aal4326) [Medline](#)
35. D. A. Dougherty, Cation- $\pi$  interactions in chemistry and biology: A new view of benzene, Phe, Tyr, and Trp. *Science* **271**, 163–168 (1996). [doi:10.1126/science.271.5246.163](https://doi.org/10.1126/science.271.5246.163) [Medline](#)
36. S. H. Heinemann, H. Terlau, K. Imoto, Molecular basis for pharmacological differences between brain and cardiac sodium channels. *Pflugers Arch.* **422**, 90–92 (1992). [doi:10.1007/BF00381519](https://doi.org/10.1007/BF00381519) [Medline](#)
37. P. H. Backx, D. T. Yue, J. H. Lawrence, E. Marban, G. F. Tomaselli, Molecular localization of an ion-binding site within the pore of mammalian sodium channels. *Science* **257**, 248–251 (1992). [doi:10.1126/science.1321496](https://doi.org/10.1126/science.1321496) [Medline](#)
38. J. R. Walker, P. A. Novick, W. H. Parsons, M. McGregor, J. Zablocki, V. S. Pande, J. Du Bois, Marked difference in saxitoxin and tetrodotoxin affinity for the human nociceptive voltage-gated sodium channel (Na<sub>v</sub>1.7). *Proc. Natl. Acad. Sci. U.S.A.* **109**, 18102–18107 (2012). [doi:10.1073/pnas.1206952109](https://doi.org/10.1073/pnas.1206952109) [Medline](#)
39. J. Zhang, W. Mao, Y. Ren, R. N. Sun, N. Yan, H. Gong, Simulating the ion permeation and ion selection for a eukaryotic voltage-gated sodium channel Na<sub>v</sub>PaS. *Protein Cell* **9**, 580–585 (2018). [Medline](#)
40. M. Noda, H. Suzuki, S. Numa, W. Stühmer, A single point mutation confers tetrodotoxin and saxitoxin insensitivity on the sodium channel II. *FEBS Lett.* **259**, 213–216 (1989). [doi:10.1016/0014-5793\(89\)81531-5](https://doi.org/10.1016/0014-5793(89)81531-5) [Medline](#)
41. H. Terlau, S. H. Heinemann, W. Stühmer, M. Pusch, F. Conti, K. Imoto, S. Numa, Mapping the site of block by tetrodotoxin and saxitoxin of sodium channel II. *FEBS Lett.* **293**, 93–96 (1991). [doi:10.1016/0014-5793\(91\)81159-6](https://doi.org/10.1016/0014-5793(91)81159-6) [Medline](#)
42. K. J. Kontis, A. L. Goldin, Site-directed mutagenesis of the putative pore region of the rat IIA sodium channel. *Mol. Pharmacol.* **43**, 635–644 (1993). [Medline](#)
43. H. Nakayama, Y. Hatanaka, E. Yoshida, K. Oka, M. Takanohashi, Y. Amano, Y. Kanaoka, Photolabeled sites with a tetrodotoxin derivative in the domain III and IV of the electroplax sodium channel. *Biochem. Biophys. Res. Commun.* **184**, 900–907 (1992). [doi:10.1016/0006-291X\(92\)90676-C](https://doi.org/10.1016/0006-291X(92)90676-C) [Medline](#)
44. J. L. Penzotti, H. A. Fozzard, G. M. Lipkind, S. C. Dudley Jr., Differences in saxitoxin and tetrodotoxin binding revealed by mutagenesis of the Na<sup>+</sup> channel outer vestibule. *Biophys. J.* **75**, 2647–2657 (1998). [doi:10.1016/S0006-3495\(98\)77710-0](https://doi.org/10.1016/S0006-3495(98)77710-0) [Medline](#)
45. J. L. Penzotti, G. Lipkind, H. A. Fozzard, S. C. Dudley Jr., Specific neosaxitoxin interactions with the Na<sup>+</sup> channel outer vestibule determined by mutant cycle analysis. *Biophys. J.* **80**, 698–706 (2001). [doi:10.1016/S0006-3495\(01\)76049-3](https://doi.org/10.1016/S0006-3495(01)76049-3) [Medline](#)
46. G. Choudhary, L. Shang, X. Li, S. C. Dudley Jr., Energetic localization of saxitoxin in its channel binding site. *Biophys. J.* **83**, 912–919 (2002). [doi:10.1016/S0006-3495\(02\)75217-X](https://doi.org/10.1016/S0006-3495(02)75217-X) [Medline](#)
47. G. Choudhary, M. Yotsu-Yamashita, L. Shang, T. Yasumoto, S. C. Dudley Jr., Interactions of the C-11 hydroxyl of tetrodotoxin with the sodium channel outer vestibule. *Biophys. J.* **84**, 287–294 (2003). [doi:10.1016/S0006-3495\(03\)74849-8](https://doi.org/10.1016/S0006-3495(03)74849-8) [Medline](#)
48. E. Carbonneau, K. Vijayaragavan, M. Chahine, A tryptophan residue (W736) in the amino-terminus of the P-segment of domain II is involved in pore formation in Na<sub>v</sub>1.4 voltage-gated sodium channels. *Pflugers Arch.* **445**, 18–24 (2002). [doi:10.1007/s00424-002-0887-9](https://doi.org/10.1007/s00424-002-0887-9) [Medline](#)
49. Z. Yan, Q. Zhou, L. Wang, J. Wu, Y. Zhao, G. Huang, W. Peng, H. Shen, J. Lei, N. Yan, Structure of the Na<sub>v</sub>1.4- $\beta$ 1 complex from electric eel. *Cell* **170**, 470–482.e11 (2017). [doi:10.1016/j.cell.2017.06.039](https://doi.org/10.1016/j.cell.2017.06.039) [Medline](#)
50. J. Gilchrist, S. Das, F. Van Petegem, F. Bosmans, Crystallographic insights into sodium-channel modulation by the  $\beta$ 4 subunit. *Proc. Natl. Acad. Sci. U.S.A.* **110**, E5016–E5024 (2013). [doi:10.1073/pnas.1314557110](https://doi.org/10.1073/pnas.1314557110) [Medline](#)
51. J. Lei, J. Frank, Automated acquisition of cryo-electron micrographs for single particle reconstruction on an FEI Tecnai electron microscope. *J. Struct. Biol.* **150**, 69–80 (2005). [doi:10.1016/j.jsb.2005.01.002](https://doi.org/10.1016/j.jsb.2005.01.002) [Medline](#)
52. S. Q. Zheng, E. Palovcak, J.-P. Armache, K. A. Verba, Y. Cheng, D. A. Agard, MotionCor2: Anisotropic correction of beam-induced motion for improved cryo-electron microscopy. *Nat. Methods* **14**, 331–332 (2017). [doi:10.1038/nmeth.4193](https://doi.org/10.1038/nmeth.4193) [Medline](#)
53. T. Grant, N. Grigorieff, Measuring the optimal exposure for single particle cryo-EM using a 2.6 Å reconstruction of rotavirus VP6. *eLife* **4**, e06980 (2015). [doi:10.7554/eLife.06980](https://doi.org/10.7554/eLife.06980) [Medline](#)
54. K. Zhang, Gctf: Real-time CTF determination and correction. *J. Struct. Biol.* **193**, 1–12 (2016). [doi:10.1016/j.jsb.2015.11.003](https://doi.org/10.1016/j.jsb.2015.11.003) [Medline](#)
55. S. H. Scheres, A Bayesian view on cryo-EM structure determination. *J. Mol. Biol.* **415**, 406–418 (2012). [doi:10.1016/j.jmb.2011.11.010](https://doi.org/10.1016/j.jmb.2011.11.010) [Medline](#)
56. S. H. Scheres, RELION: Implementation of a Bayesian approach to cryo-EM structure determination. *J. Struct. Biol.* **180**, 519–530 (2012). [doi:10.1016/j.jsb.2012.09.006](https://doi.org/10.1016/j.jsb.2012.09.006) [Medline](#)
57. S. H. Scheres, Semi-automated selection of cryo-EM particles in RELION-1.3. *J. Struct. Biol.* **189**, 114–122 (2015). [doi:10.1016/j.jsb.2014.11.010](https://doi.org/10.1016/j.jsb.2014.11.010) [Medline](#)
58. D. Kimanius, B. O. Forsberg, S. H. Scheres, E. Lindahl, Accelerated cryo-EM structure determination with parallelisation using GPUs in RELION-2. *eLife* **5**, e18722 (2016). [doi:10.7554/eLife.18722](https://doi.org/10.7554/eLife.18722) [Medline](#)
59. P. B. Rosenthal, R. Henderson, Optimal determination of particle orientation, absolute hand, and contrast loss in single-particle electron cryomicroscopy. *J. Mol. Biol.* **333**, 721–745 (2003). [doi:10.1016/j.jmb.2003.07.013](https://doi.org/10.1016/j.jmb.2003.07.013) [Medline](#)
60. S. Chen, G. McMullan, A. R. Faruqi, G. N. Murshudov, J. M. Short, S. H. W. Scheres, R. Henderson, High-resolution noise substitution to measure overfitting and validate resolution in 3D structure determination by single particle electron cryomicroscopy. *Ultramicroscopy* **135**, 24–35 (2013). [doi:10.1016/j.ultramic.2013.06.004](https://doi.org/10.1016/j.ultramic.2013.06.004) [Medline](#)
61. E. F. Pettersen, T. D. Goddard, C. C. Huang, G. S. Couch, D. M. Greenblatt, E. C. Meng, T. E. Ferrin, UCSF Chimera—A visualization system for exploratory research and analysis. *J. Comput. Chem.* **25**, 1605–1612 (2004). [doi:10.1002/jcc.20084](https://doi.org/10.1002/jcc.20084) [Medline](#)
62. P. Emsley, B. Lohkamp, W. G. Scott, K. Cowtan, Features and development of Coot. *Acta Crystallogr. D Biol. Crystallogr.* **66**, 486–501 (2010). [doi:10.1107/S0907444910007493](https://doi.org/10.1107/S0907444910007493) [Medline](#)
63. P. D. Adams, P. V. Afonine, G. Bunkóczi, V. B. Chen, I. W. Davis, N. Echols, J. J. Headd, L.-W. Hung, G. J. Kapral, R. W. Grosse-Kunstleve, A. J. McCoy, N. W. Moriarty, R. Oeffner, R. J. Read, D. C. Richardson, J. S. Richardson, T. C. Terwilliger, P. H. Zwart, PHENIX: A comprehensive Python-based system for macromolecular structure solution. *Acta Crystallogr. D Biol. Crystallogr.* **66**, 213–221 (2010). [doi:10.1107/S0907444909052925](https://doi.org/10.1107/S0907444909052925) [Medline](#)
64. A. Amunts, A. Brown, X. C. Bai, J. L. Llácer, T. Hussain, P. Emsley, F. Long, G. Murshudov, S. H. W. Scheres, V. Ramakrishnan, Structure of the yeast mitochondrial large ribosomal subunit. *Science* **343**, 1485–1489 (2014). [doi:10.1126/science.1249410](https://doi.org/10.1126/science.1249410) [Medline](#)
65. K. Dong, A single amino acid change in the para sodium channel protein is associated with knockdown-resistance (kdr) to pyrethroid insecticides in German cockroach. *Insect Biochem. Mol. Biol.* **27**, 93–100 (1997). [doi:10.1016/S0965-1748\(96\)00082-3](https://doi.org/10.1016/S0965-1748(96)00082-3) [Medline](#)
66. G. Feng, P. Deák, M. Chopra, L. M. Hall, Cloning and functional analysis of TipE, a novel membrane protein that enhances *Drosophila para* sodium channel function. *Cell* **82**, 1001–1011 (1995). [doi:10.1016/0092-8674\(95\)90279-1](https://doi.org/10.1016/0092-8674(95)90279-1) [Medline](#)
67. W. L. DeLano, The PyMOL Molecular Graphics System (2002); [www.pymol.org](http://www.pymol.org).

#### ACKNOWLEDGMENTS

We thank Xiaomin Li (Tsinghua University) for technical support during EM image acquisition. We thank Ke Dong (Michigan State University) for sharing BgNav1 (Na<sub>v</sub>Bg) and TipE constructs. **Funding:** This work was funded by the National Key Basic Research (973) Program (2015CB910101 to N.Y.) and the National Key R&D Program (2016YFA0500402 to N.Y. and 2016YFA0501100 to J.L.) from Ministry of Science and Technology of China, the National Natural Science Foundation of China (projects 31621092, 31630017, and 31611130036 to N. Y.), the Australian Research Council (DP160104411), and the Australian National Health & Medical Research Council (Principal Research Fellowship and Program Grant APP1072113 to G.F.K.). We thank the Tsinghua University Branch of China National Center for Protein Sciences (Beijing) for providing the cryo-EM facility

support. We thank the computational facility support on the cluster of Bio-Computing Platform (Tsinghua University Branch of China National Center for Protein Sciences Beijing) and the “Explorer 100” cluster system of Tsinghua National Laboratory for Information Science and Technology. N.Y. is supported by the Shirley M. Tilghman endowed professorship from Princeton University.

**Ethics statement:** This study was carried out in accordance with the recommendations in the Australian code of practice for the care and use of animals for scientific purposes (8th Ed., 2013). The protocol for *Xenopus laevis* studies was approved by the Animal Ethics Committee of The University of Queensland (approval number QBI/059/13/ARC/NHMRC). Surgeries for harvesting *Xenopus laevis* oocytes with recovery end-point were performed under anesthesia (animals exposed to tank filled with 1.3 mg/ml of MS-222), with a minimum of three months between surgeries. **Author contributions:** N.Y., G.F.K., and Q.Z. conceived the project. H.S., Q.Z., Z.L., J.Y., X.P., J.W., B.C., J.J.S., Y.K.Y.C., and J.L. performed the experiments. All authors contributed to data analysis. N.Y., G.F.K., Q.Z., and H.S. wrote the manuscript. **Competing interests:** The authors declare no competing interests. **Data and materials availability:** The atomic coordinates for Na<sub>2</sub>PaS-Dc1a complex, Na<sub>2</sub>PaS-Dc1a-TTX complex, and Na<sub>2</sub>PaS-Dc1a-STX complex have been deposited in the Protein Data Bank (<http://www.rcsb.org>) with the accession code 6A90, 6A95 and 6A91 respectively. The EM maps have been deposited in EMDB (<https://www.ebi.ac.uk/pdbe/emdb/>) with accession code EMD-6995, EMD-6997 and EMD-6996 respectively.

#### SUPPLEMENTARY MATERIALS

[www.sciencemag.org/cgi/content/full/science.aau2596/DC1](http://www.sciencemag.org/cgi/content/full/science.aau2596/DC1)

Figs. S1 to S10

Table S1

References

22 May 2018; accepted 17 July 2018

Published online 26 July 2018

10.1126/science.aau2596

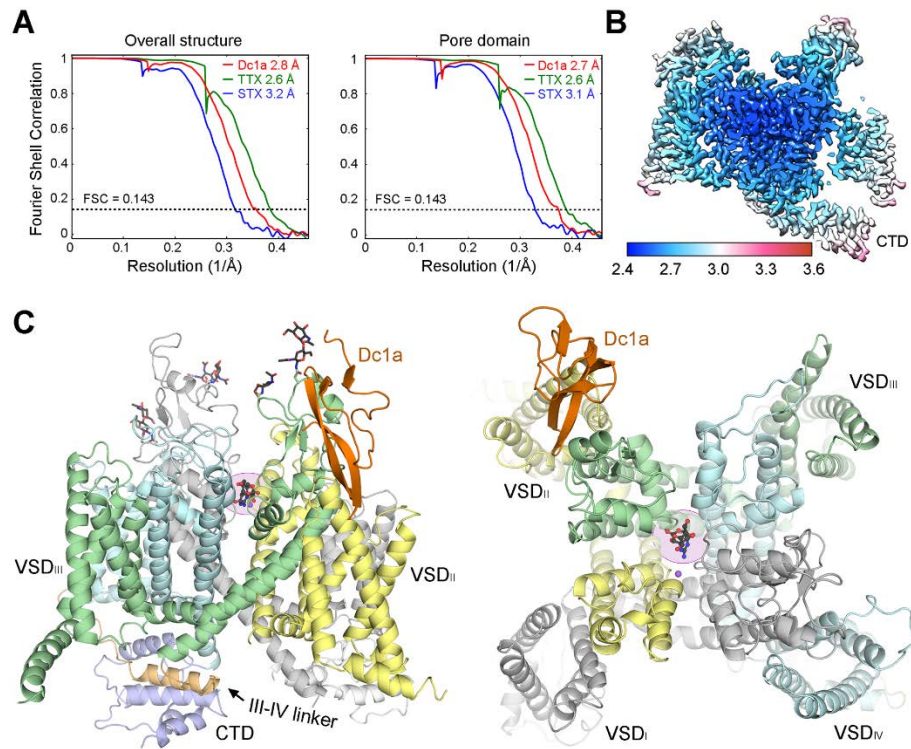


**Fig. 1. Structures of the complex between Na<sub>v</sub>PaS and the peptide toxin Dc1a with or without TTX/STX.** (A) Gold-standard Fourier shell correlation (FSC) curves for the 3D EM reconstructions of the Na<sub>v</sub>PaS-Dc1a complex in the absence or presence of TTX or STX. Left: FSC curves for the overall structures. Right: FSC curves for the pore domains that were masked during post-processing. (B) Local resolution map of the Na<sub>v</sub>PaS-Dc1a-TTX complex. The map was estimated with RELION 2.0 and generated in Chimera. (C) Overall structure of the Na<sub>v</sub>PaS-Dc1a-TTX complex. Side view and top view are shown. Since the three overall structures are nearly identical, only one is shown as a representative. The four repeats in Na<sub>v</sub>PaS are shown in different colors and Dc1a is colored orange. The sugar moieties are shown as black sticks. TTX, shown as black ball-and-sticks, is highlighted by the pink shade. The putative Na<sup>+</sup> ion is shown as purple sphere. All structure figures were prepared with PyMol (67).

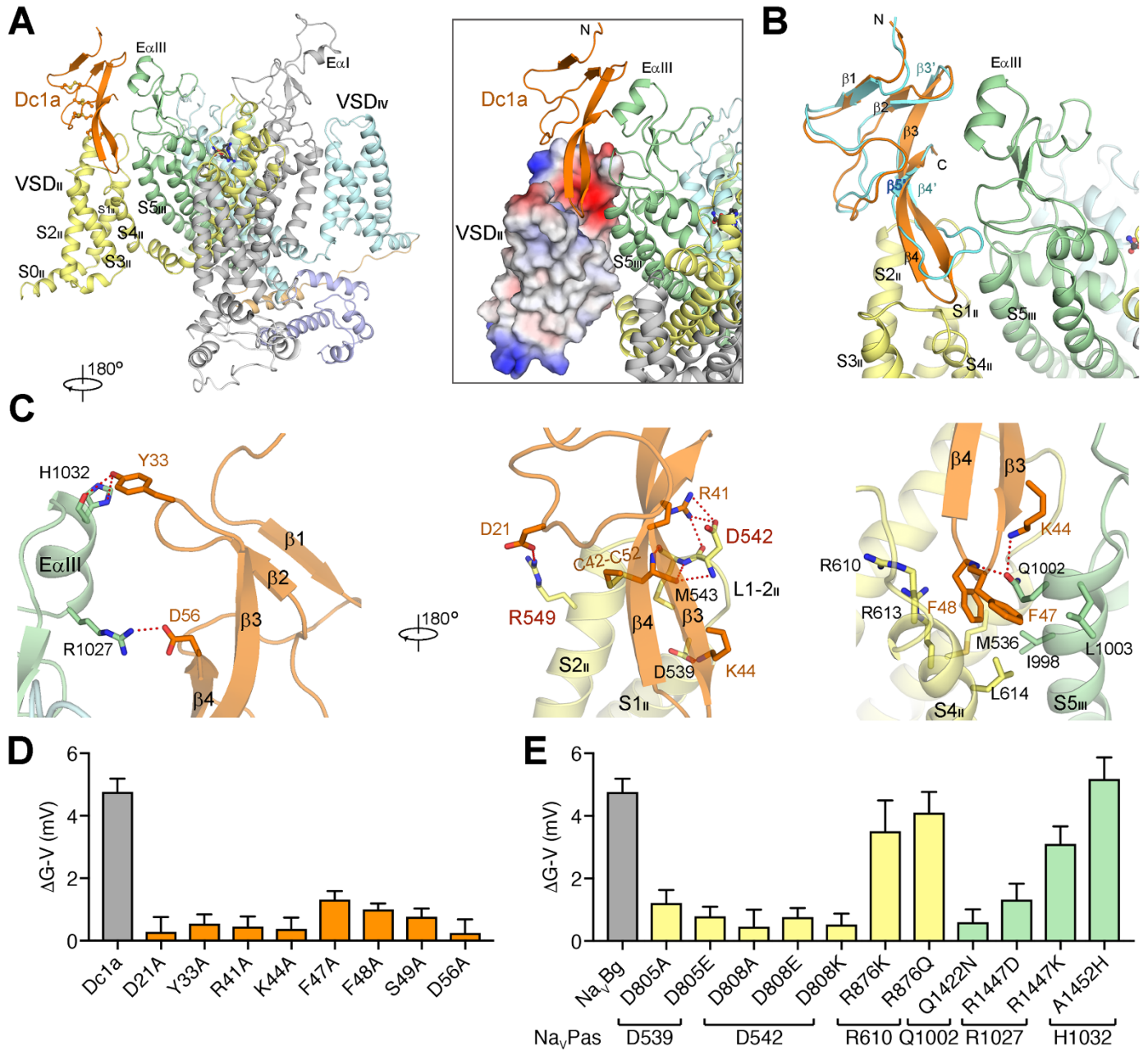


**Fig. 2. The interaction between Dc1a and Na<sub>v</sub>PaS.** (A) Dc1a inserts into the extracellular cavity between VSD<sub>II</sub> and the pore elements of repeat III. The four disulfide bonds in Dc1a are shown as ball and sticks. E $\alpha$ III: The extracellular  $\alpha$  helix in Repeat III. Inset: VSD<sub>II</sub> is shown as surface electrostatic potential calculated in PyMol. (B) The conformational changes of Dc1a upon binding to Na<sub>v</sub>PaS. The NMR-determined structure of free Dc1a (cyan) contains five short  $\beta$ -strands, with  $\beta$ 4 and  $\beta$ 5 connected by a flexible linker. When binding to Na<sub>v</sub>PaS, the segments containing  $\beta$ 3- $\beta$ 5 (labeled as  $\beta$ 3'- $\beta$ 5' to be distinguished from those in the complex structure) become rigidified to form an elongated  $\beta$  hairpin. (C) Specific interactions between Dc1a and Na<sub>v</sub>PaS. Electrostatic interactions are shown as red dashed lines. The three panels illustrate the contacts from top to bottom. Left: Interactions between Dc1a and the extracellular segments above the pore domain in Repeat III of Na<sub>v</sub>PaS. Middle: Interactions between Dc1a and the L1-2<sub>II</sub> loop (the loop that connects the S1 and S2 segments in VSD<sub>II</sub>). Asp542 and Arg549, which are not conserved in mammalian Na<sub>v</sub> channels, are highlighted with red labels. Right: Interactions of Dc1a with S4<sub>II</sub> and S5<sub>III</sub>. (D and E) Structure-guided mutagenesis characterizations corroborate the structural observations. (D) Shift in G-V curve ( $\Delta_{G-V}$ ) for Na<sub>v</sub>Bg induced by wild-type (WT) and mutant Dc1a peptides (1  $\mu$ M). WT Dc1a is shown in grey while mutants are colored orange ( $n = 5-7$ ). (E) Shift in G-V curve ( $\Delta_{G-V}$ ) for WT and mutant Na<sub>v</sub>Bg channels induced by WT Dc1a (1  $\mu$ M). Mutants are labeled according to the sequence of WT Na<sub>v</sub>Bg, with corresponding Na<sub>v</sub>PaS numbering below. WT channel is shown in grey, while residues located in VSD<sub>II</sub> and S5-S6<sub>III</sub> are colored yellow and green, respectively ( $n = 5-6$ ). All data are mean  $\pm$  s.e.m. Please refer to figs. S6 to S9 for experimental details.

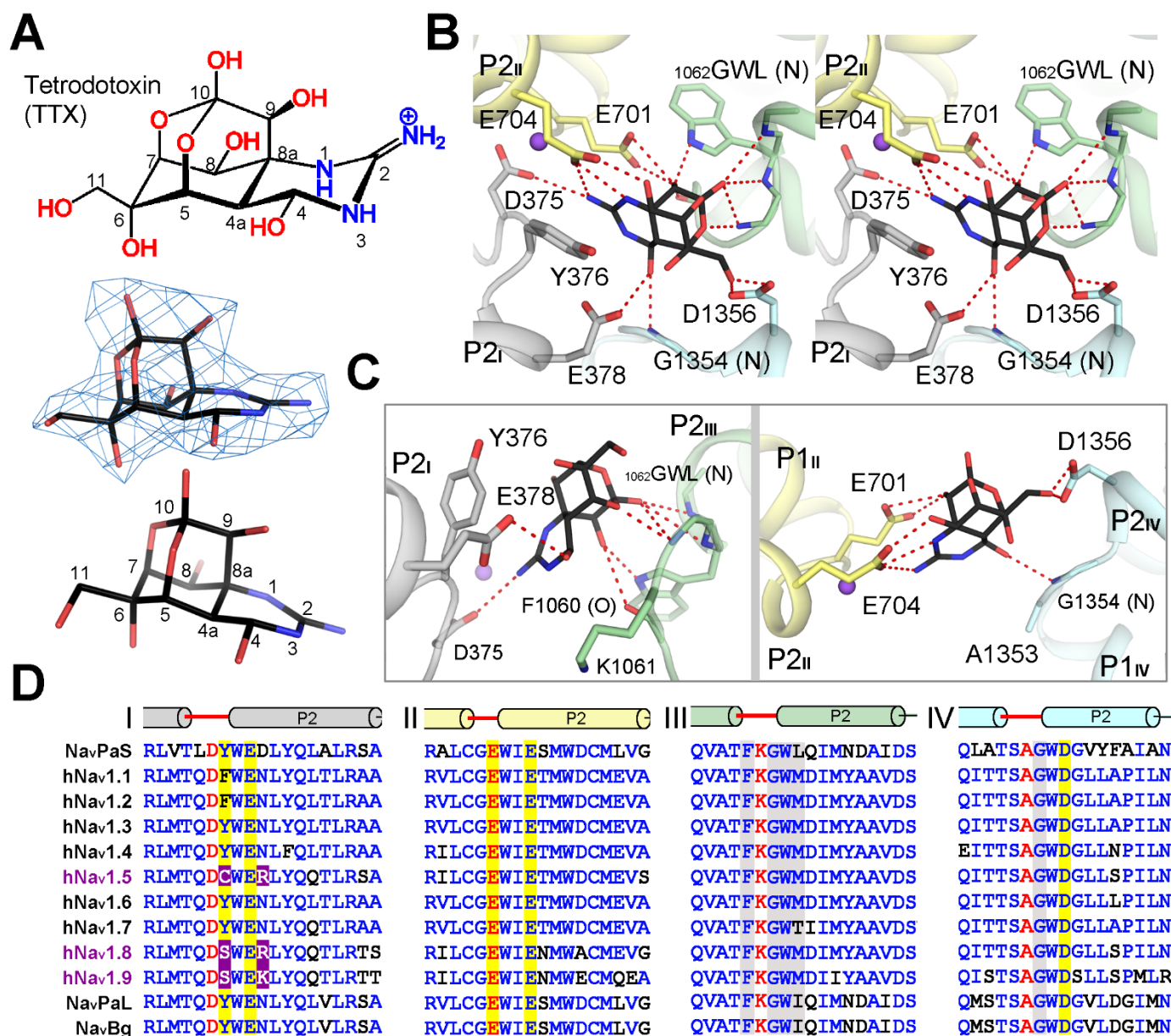


**Fig. 3. Specific interactions between  $\text{Na}_v\text{PaS}$  and TTX.** (A) Structure of TTX. Top: The chemical structure of TTX. Middle: The density for TTX, shown as blue mesh, is contoured at  $10 \sigma$ . Bottom: The resolved 3D structure of TTX bound to  $\text{Na}_v\text{PaS}$ . (B) TTX is specifically coordinated by acidic residues and backbone amides at the outer vestibule of the SF. A stereo view from the extracellular side is shown. The putative  $\text{Na}^+$  ion is shown as purple sphere. (C) The detailed coordination of TTX by residues from the diagonal repeats shown in side views. (D) Sequence alignment of the SF elements and P2 helices in the four channel repeats. The panel is adapted from the reported sequence alignment (34). The residues whose side chains are involved in TTX coordination via polar interactions are shaded yellow. The residues whose backbone amides bind to the oxygen anion are shaded grey. In the TTX-resistant  $\text{Na}_v$  subtypes, the equivalent of Tyr376, which appears to form  $\pi$ -cation interaction with the 1,2,3-guanidinium of TTX, is Cys ( $\text{Na}_v1.5$ ) or Ser ( $\text{Na}_v1.8$  and  $\text{Na}_v1.9$ ).

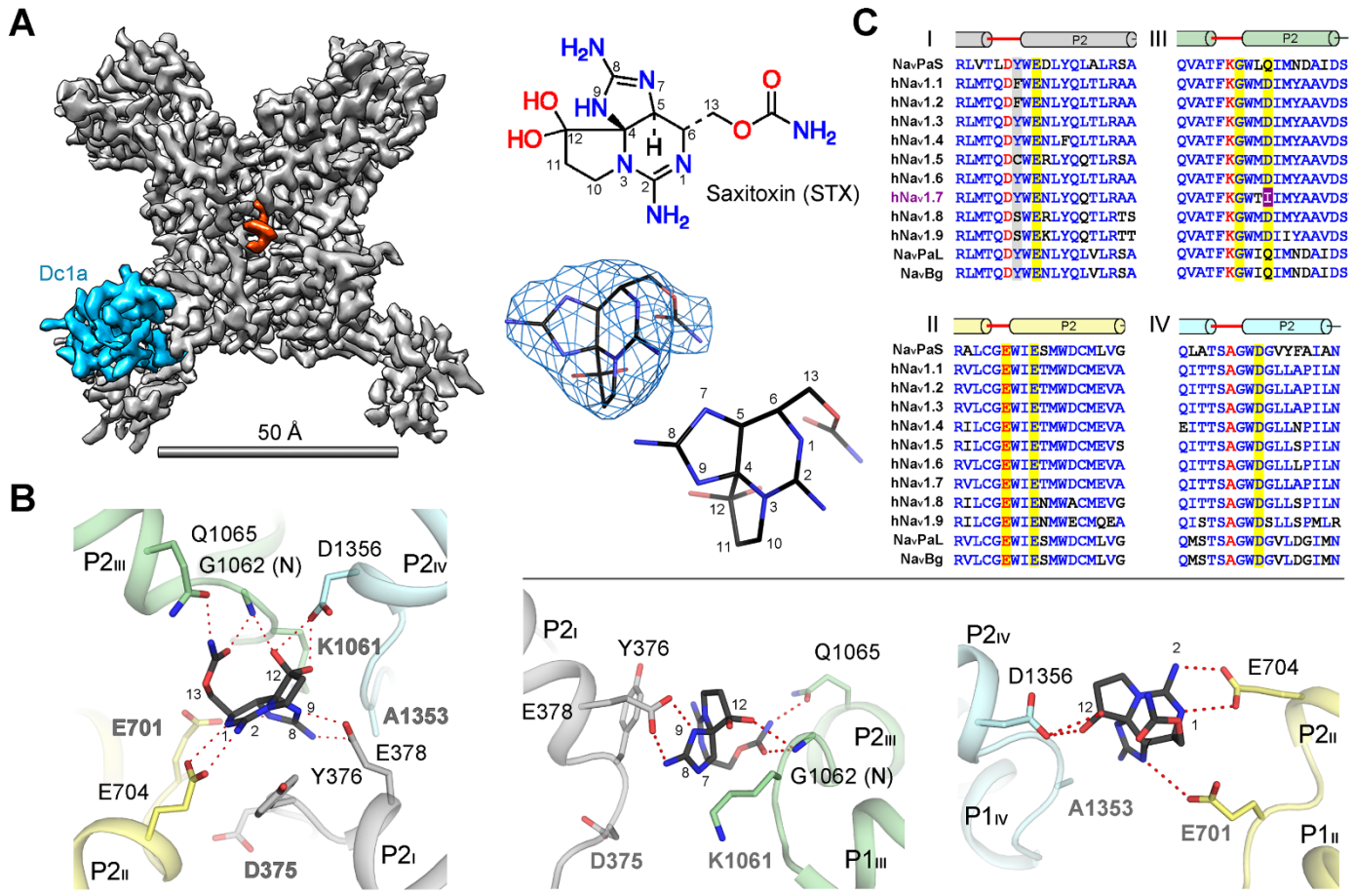


**Fig. 4. Specific interactions between NavPaS and STX.** (A) STX is well resolved in the 3.1 Å-resolution EM reconstruction of the central domain of NavPaS. Left: An extracellular view of the overall EM map. The densities corresponding to STX and Dc1a are colored red and cyan, respectively. Right: Chemical structure (top) and 3D structure (bottom) of the NavPaS-bound STX. Shown in the middle is the density (blue mesh) for the bound STX at 5  $\sigma$ . (B) STX is specifically coordinated by charged and polar residues from the four repeats at the outer vestibule of the SF. Left: STX tightly blocks the entrance to the SF. An extracellular view is shown. Middle and right: Side views of the coordination of STX by residues from the diagonal repeats. (C) Sequence alignment of the SF elements and P2 helices in the four repeats. Similar to Fig. 3D, the residues that participate in STX coordination via polar interactions are shaded yellow. Tyr376, which forms a  $\pi$ -cation interaction with the 1,2,3-guanidinium of STX, is shaded grey. The locus corresponding to NavPaS-Q1065 is Ile in human Nav1.7, which has a much lower affinity for STX than other subtypes of human Nav channels in which this locus is occupied by Asp.

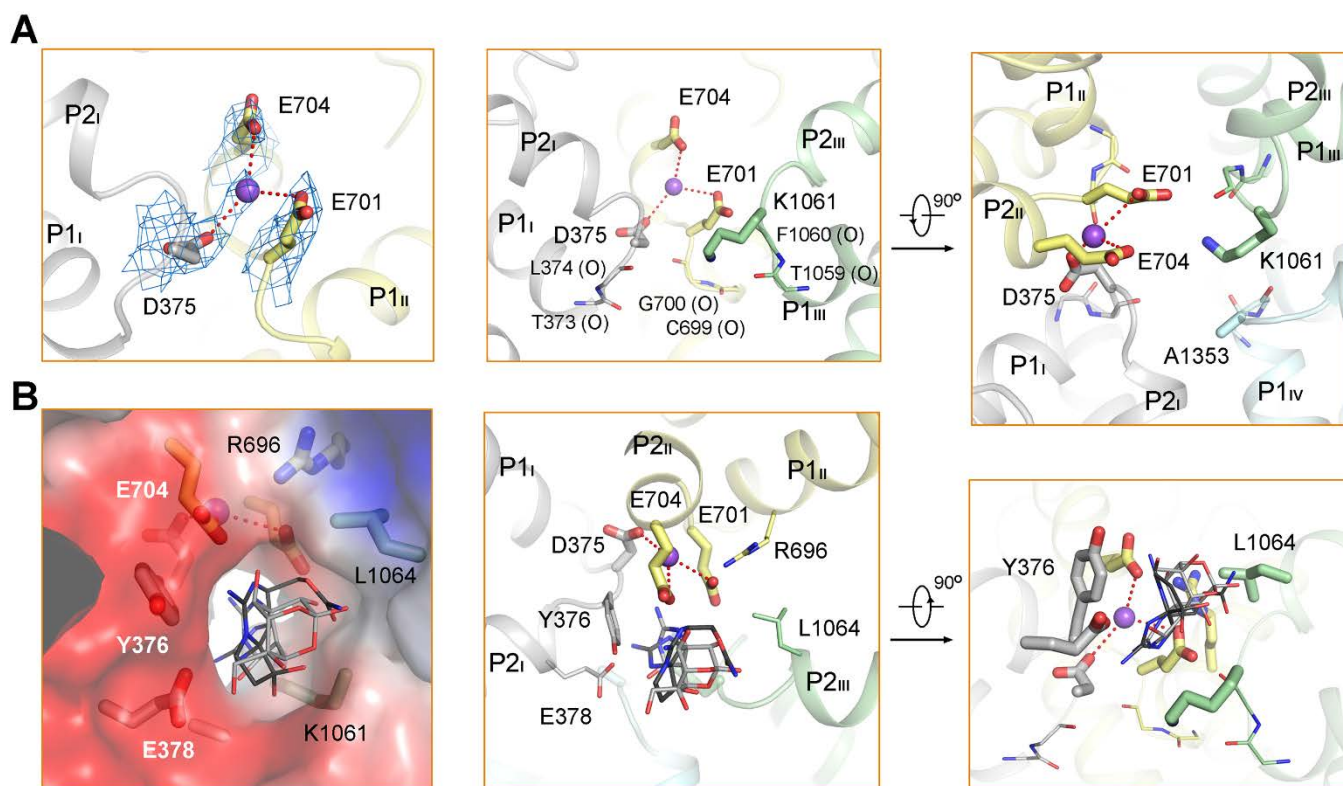


**Fig. 5. Molecular mechanism for pore blockade by TTX/STX.** (A) A potential  $\text{Na}^+$  binding site within SF. The carboxylate groups of DE and an invariant Glu on P2<sub>II</sub> together constitute a potential  $\text{Na}^+$  binding site (designated the DEE site). Left: A density surrounded by three carboxylate groups may belong to a bound  $\text{Na}^+$  ion in the structure of  $\text{Na}_v\text{PaS-Dc1a}$ , which was purified in the presence of 300 mM NaCl. A similar density is observed in the EM map for  $\text{Na}_v\text{PaS-Dc1a-TTX}$ . Please refer to fig. S4C. Middle and right: Asymmetric coordination of the  $\text{Na}^+$  ion within the SF vestibule. Side and top views of the SF vestibule are shown. Repeat IV is omitted in the side view for visual clarity. The carbonyl oxygens that constitute the potential inner site for  $\text{Na}^+$  within the SF are shown as thin sticks. The structural observation is consistent with a recent MD simulation analysis of the  $\text{Na}^+$  permeation path (39). See fig. S10 for details. (B) TTX/STX completely blocks access of  $\text{Na}^+$  to the DEE site from the extracellular side. Left: The asymmetric chemical composition of the SF outer vestibule determines the permeation path for  $\text{Na}^+$ . Shown here is a semi-transparent presentation of the electrostatic surface potential of the entrance to the SF viewed from the extracellular side. The residues that give rise to the surface feature are shown in sticks. TTX and STX are shown as silver and black sticks, respectively. Middle and right: The relative position of TTX/STX with respect to the bound  $\text{Na}^+$  ion. Placement of TTX/STX at the outer mouth to SF prevents the access of  $\text{Na}^+$  to the DEE site from the extracellular side.

## Structural basis for the modulation of voltage-gated sodium channels by animal toxins

Huaizong Shen, Zhangqiang Li, Yan Jiang, Xiaojing Pan, Jianping Wu, Ben Cristofori-Armstrong, Jennifer J. Smith, Yanni K. Y. Chin, Jianlin Lei, Qiang Zhou, Glenn F. King and Nieng Yan

published online July 26, 2018

### ARTICLE TOOLS

<http://science.sciencemag.org/content/early/2018/07/25/science.aau2596>

### SUPPLEMENTARY MATERIALS

<http://science.sciencemag.org/content/suppl/2018/07/25/science.aau2596.DC1>

### REFERENCES

This article cites 65 articles, 20 of which you can access for free  
<http://science.sciencemag.org/content/early/2018/07/25/science.aau2596#BIBL>

### PERMISSIONS

<http://www.sciencemag.org/help/reprints-and-permissions>

Use of this article is subject to the [Terms of Service](#)